Implementation of a Multi-resolution Analysis Method to Characterize Multi-Scale Wave Structures in Lidar Data

Samuel Trémoulu[1], Fabrice Chane Ming[1], Alain Hauchecorne[2,4], Sergey Khaykin[2], Mathieu Ratynski[3], and Philippe Keckhut[2]

[1]LACy, CNRS/Météo-France, UMR 8105, Université de La Réunion, 97744 Saint-Denis de La Réunion, France
[2]LATMOS-IPSL, CNRS/INSU, UMR 8190, Université de Paris-Saclay, 78280 Guyancourt, France
[3]Rosenstiel School of Marine and Atmospheric Science (RSMAS), University of Miami, Miami, Florida
[4]Gordien Strato, 78280 Guyancourt, France

Correspondence: Samuel Trémoulu (samuel.tremoulu@univ-reunion.fr)

Abstract. ~~This study introduces~~ Extracting gravity wave (GW) perturbations from atmospheric observations relies on background removal techniques whose results may differ depending on the observational type and the spectral characteristics of the chosen method. This variability complicates the intercomparison of GW properties across instruments, sites, and studies. To address this issue, we implement and evaluate a processing method based on ~~multi-resolution~~ multiresolution analysis (MRA)~~to~~ , designed to extract and characterize the multi-scale ~~structures of gravity waves (GWs) with vertical wavelengths less than 13 in lidar vertical profiles of~~ structure of GWs in lidar temperature and wind ~~in the middle atmosphere~~profiles. Unlike standard filtering techniques, MRA provides a scale-resolved and energy-conserving decomposition of atmospheric signals. The MRA approach is evaluated against ~~conventional techniques, including~~ three widely used techniques—sliding polynomial fitting, spectral filtering, and nighttime temporal averaging~~,~~ —and applied to a case study of ~~GWs observed on November~~ intense GW activity observed on 20~~, 2023. Among these methods, MRA demonstrates superior performance by enhancing~~ November 2023 above La Réunion. By decomposing the signal into dyadic vertical wavelength bands, MRA enhances the signal-to-noise ratio ~~through signal decomposition and selective filtering. This targeted filtering~~ and improves the detection ~~and extraction~~ of GW-induced perturbations, particularly for dominant vertical wavelengths around 5 km. In terms of ~~GW~~ gravity wave potential energy (GWPE), ~~the MRA-based method yields values comparable to those derived from~~ MRA agrees within 30 % with the variance method ~~, except at the stratopause, where it estimates nearly twice the GWPE. However, the variance-based estimate remains within the MRA-derived confidence interval, indicating good agreement. In contrast, the Butterworth low-pass filter produces energy densities an order of magnitude higher than the variance method, suggesting possible overestimation of perturbation amplitudes. Polynomial fitting and nighttime mean methods appear insensitive to small-scale GW structures near the stratopause, where wave dissipation may occur~~throughout the middle atmosphere. Conventional techniques show larger discrepancies, with relative differences of 40 % (spectral filtering) up to more than 100 % (nighttime averaging), especially in the mesosphere where noise dominates. For gravity wave kinetic energy (GWKE), spectral filtering and sliding polynomial fitting overestimate MRA values by approximately 60 % in the stratosphere and lower mesosphere, while nighttime averaging performs reasonably well only in the troposphere (20 % higher) but diverges at higher altitudes. Beyond energy estimation, ~~the MRA method offers a distinct advantage for analyzing GW propagation and scale interactions due to its~~

~~multi-scale decomposition capability. It reveals GW features and structures that remain obscured by common techniques, establishing it as a valuable tool for advancing the study of GW dynamics in the middle atmosphere.~~ MRA provides a unique capability to compute kinetic and potential energy profiles for tunable vertical wavelength bands, enabling the characterization of vertical and temporal evolution and interactions between different GW scales. These results establish MRA as a robust and complementary tool for improving GW analyses from lidar measurements, with promising applications to long-term climatologies and multi-instrument observational strategies.

1 Introduction

Atmospheric gravity waves (~~GWs~~GW) have become a major focus of research in recent years because of their significant effects on atmospheric dynamics and chemistry ~~, as well as the limitations in resolving small-scale structures in current numerical weather prediction and climate models (Fritts and Alexander, 2003)~~(Fritts and Alexander, 2003; Medvedev and Yiğit, 2019). As they propagate, GWs strongly influence large-scale atmospheric processes by modulating both horizontal and vertical momentum fluxes~~(e.g. , the Brewer-Dobson circulation , the pole-to-pole circulation). They also play a crucial role in vertically coupling the lower and middle atmosphere~~. It is commonly assumed that they have a leading-order influence on the mean circulation in the mesosphere and lower thermosphere and that they also impact the tropospheric and stratospheric circulation (Andrews et al., 1987; Holton and Alexander, 2000; Vallis, 2017). Beyond the atmospheric mean circulation, GW impacts also extend to atmospheric variability and predictability from subseasonal to decadal time scales. Hence it is essential that regional and global atmospheric models describe GWs and their effects with reliable accuracy (Achatz et al., 2024). The ongoing improvement of model resolutions leads to an increasing fraction of the GW spectrum that can be simulated explicitly. Yet, even the highest-resolution numerical weather predictions (NWP) still cannot accurately represent the full GW spectrum, so that they will depend on parameterizations for some time to come (Kruse et al., 2022; Polichtchouk et al., 2022).

Over the past four decades, lidars have proven to be invaluable tools for observing and characterizing vertically propagating GWs in the middle atmosphere ~~(e.g., Chanin and Hauchecorne, 1981; Gardner et al., 1993; Wilson et al., 1991; Whiteway and Carswell, 19~~

~~. These studies highlight the capability of lidar observations to infer~~ (Chanin and Hauchecorne, 1981; Gardner et al., 1993; Wilson et al., 19

. Lidar observations are capable of inferring long-term trends ~~in GW activity~~of the middle atmosphere (Li et al., 2011; Kishore et al., 2014;

. In particular, lidars provide unique, high-resolution dynamical measurements of temperature and wind across the middle atmosphere, with excellent temporal and vertical resolution. Such measurements are widely used to investigate GW propagation, especially in the mesosphere and lower thermosphere (MLT) region ~~(Liu et al., 2009; Placke et al., 2013; Lu et al., 2015, 2017; Kaifler et al~~

(Liu et al., 2009; Placke et al., 2013; Lu et al., 2015; Kaifler et al., 2015; Chen et al., 2016; Lu et al., 2017; Chane Ming et al., 2023; Vada

. However, lidars typically produce one-dimensional, nighttime vertical profiles, which limits their ability to resolve the horizontal structure and intrinsic properties of atmospheric waves.

Retrieving GW activity from observations requires isolating wave-induced perturbations from the estimated background state. The wave signal itself spans a broad spectral range, including contributions from tides, planetary waves, and GWs. Depending on the observational technique and data processing approach, the fluctuating dynamical component may be attributed primarily to GWs. However, a major challenge lies in effectively distinguishing large-scale GWs from other overlapping wave types. Over the past several decades, various methods have been developed to extract GW perturbations from lidar-derived temperature and wind profiles by removing the background signal. A commonly used technique involves subtracting a nightly mean profile, considered representative of the background, from each individual profile (Gardner et al., 1989; Rauthe et al., 2008; Ehard et al., 2014). Another widely applied method fits a polynomial function to the measured profiles to isolate the perturbation field (Whiteway and Carswell, 1995; Duck et al., 2001; Hertzog et al., 2001; Alexander et al., 2011). A further approach to separating GW contributions from large-scale atmospheric motions involves the use of high- or low-pass filters, with the cutoff wavelength determined by the specific characteristics of the filter (Chane-Ming et al., 2000). For GW analysis, high-pass filters are typically applied in the time domain to remove low-frequency components associated with large-scale waves, and in the height domain to eliminate tidal influences (Hirota, 1984; Hirota and Niki, 1985; Eckermann et al., 1995; Hertzog et al., 2001).

The sensitivity of GW detection methods varies across the wave spectrum and is also strongly influenced by the capabilities of the observing instrument, particularly lidar systems, where performance depends on factors such as laser power and collection area. In the literature, ~~GW potential energy density~~ GWPE is commonly estimated over a wide spectral range; however, comparing results across studies remains challenging. This difficulty arises from the inability to clearly distinguish variations caused by differences in methodology from those driven by geophysical variability (Ehard et al., 2015). Since the 1980s, wavelet theory has found widespread application in signal and image processing. More recently, in combination with neural networks, it has gained increasing relevance in the field of machine learning (Guo et al., 2022). Wavelet analysis is particularly well-suited for examining nonstationary, multiscale, wave-like structures, as it enables the resolution of spectral characteristics in both time and space. As such, it is a powerful tool for capturing the dynamics of GWs whose signatures are embedded in lidar-derived temperature and wind perturbations (Chane Ming et al., 2023). Orthogonal discrete wavelets further allow for the continuous tracking of spectral energy evolution with altitude, making use of the principle of energy conservation to assess vertical variations in GW activity. The linear nature of wavelet analysis also makes it well-aligned with the linear theory of GWs, which describes the wave field as a superposition of monochromatic components. Moreover, wavelet-based methods facilitate the investigation of turbulence-related processes, including energy cascades and nonlinear interactions among structures at different scales. In this context, the present study introduces a method based on the multiresolution analysis (MRA). MRA, as formalized by Mallat (1989), ~~enables the construction of orthogonal discrete wavelets~~ was developed through the concept of a filter bank with a pyramidal structure—an efficient algorithm for fast bi-band discrete wavelet decomposition and is a highly versatile tool that offers several key advantages for the analysis of GWs. It enables efficient signal denoising, multi-scale filtering, and accurate signal reconstruction, making it particularly well-suited for studying the complex, multiscale nature of GWs. GW activity in the middle atmosphere is typically quantified by calculating potential and kinetic energy densities from temperature and wind perturbations, respectively (Li et al., 2023; Brhian et al., 2024; Wüst et al., 2024). These energy densities diagnostics provide complementary insights into different aspects of GW dynamics, with kinetic energy density generally being more sensitive to low-frequency waves than potential energy (Geller and Gong, 2010).

Beyond perturbation-based methods, Mzé et al. (2014) proposed an alternative approach for estimating potential energy directly from raw lidar photon count profiles. This method builds on the variance-based technique originally developed by Hauchecorne et al. (1994), allowing GW energy to be inferred without requiring explicit background subtraction.

In this paper, we present a method based on MRA to characterize multi-scale ~~GWs in observational data, with a particular focus on lidar measurements.~~ gravity waves in lidar observations. Specifically, the study aims to compare MRA with commonly used background removal techniques such as nightly mean subtraction, sliding polynomial fitting and spectral filtering, in order to evaluate their ability to isolate GWs perturbations. The comparison focuses on key GWs properties, including vertical wavelength content, localization with height and time, and associated GWs energy.

A central motivation for this work is that, while MRA does not necessarily outperform other methods in every aspect, it provides a unique analytical framework that combines multi-scale decomposition with exact energy conservation, allowing the continuous tracking of spectral energy across different vertical scales. This capability enables the investigation of interactions between wave components of different scales, which is not possible with traditional filtering approaches that treat each scale in isolation.

All four methods are applied to the same lidar temperature and wind datasets. A systematic quantitative evaluation is conducted for the temperature profiles, based on the relative difference computed within a 10 km sliding vertical window between 10 and 70 km altitude. This provides a consistent benchmark for assessing how each filtering technique impacts GWs energy profiles. This demonstration highlights how MRA's multi-scale, energy-conserving framework can complement existing techniques for characterizing atmospheric GWs.

The paper is organized as follows: Section 2 ~~provides a description lidar data and four methods for the analysis of GWs, with an emphasis on MRA; in section 3, all methods are applied to temperature lidar data, and~~ describes the lidar datasets and the ~~characteristics as well as the comparative performance of the four methods are discussed, additionally, further applications of the MRAare demonstrated through its implementation on wind lidar data; finally, conclusions and potential~~ four filtering approaches, with a focus on the implementation of MRA and a parallel on variance based method. Section 3 presents the results of the systematic comparative analysis for temperature and wind, with a demonstration of MRA's distinctive features using wind data. Section 4 provides conclusions and outlines future applications of the MRA ~~are outlined~~technique.

2 Materials and method

2.1 Lidar data

Since 2013, the Rayleigh-Mie-Raman (RMR) lidar and the Rayleigh-Mie-Doppler (RMD) lidar have both been operating at the Maïdo Observatory on La Réunion (21°S, 55°E). The RMR lidar provides vertical profiles of temperature spanning the middle atmosphere, covering altitudes between 30 km and 90 km (Baray et al., 2013). Lidar temperature measurements are useful for the study of the middle atmosphere especially for the characterization of multi-scale dynamical processes such as mesospheric inversion layers and propagating waves (Bègue et al., 2017; Chane Ming et al., 2023). Additionally, horizontal wind velocities are produced by the RMD lidar at heights ranging from 5 km to 60 km (Khaykin et al., 2018). Lidar data are ~~mainly~~ primarily used for long-term monitoring of the middle atmosphere and ~~for calibration and validation (Cal/Val) of campaigns such the recent Cal/Val of~~ have also supported recent calibration activities, such as those conducted for the European Space Agency~~(ESA)~~ 's ADM-Aeolus satellite mission ~~for~~ dedicated to global wind observations (Ratynski et al., 2023).

Rayleigh lidar operates by measuring atmospheric density, which is directly proportional to molecular Rayleigh scattering, and calculates temperature through the downward integration of the hydrostatic law (Hauchecorne and Chanin, 1980). The light source of this lidar consists of two Quanta Ray Nd:Yag lasers. The final wavelength emitted is 355 ~~nm~~ nm with a pulse repetition at 30 ~~Hz~~ Hz and each pulse delivers 375 ~~mJ~~mJ. The backscattered signal is collected by a 1.2 ~~m~~ m diameter telescope (Gantois et al., 2024). The temperature profile is initialized at the top using a seed temperature from the NRLMSISE-00 empirical atmospheric model (Picone et al., 2002). Initially, raw Rayleigh-Mie-Raman (RMR) temperature profiles are obtained with a 1-minute integration time and a vertical resolution of 150 ~~meters~~m. To enhance the signal-to-noise ratio, vertical smoothing and time binning are applied according to the scientific objectives. For example, for nightly mean profiles available on the NDACC database, a 2 km vertical smoothing is applied using a Hanning filter to reduce noise and improve data accuracy.

The horizontal wind components are determined by measuring the Doppler shift between the emitted and backscattered light, induced by the projection of molecular or particle velocities along the laser's line of sight, which is inclined off-zenith. To capture both wind components, the laser beam is alternately directed along the zonal and meridional directions with a 45° elevation. A vertical pointing configuration is also employed to establish the zero Doppler shift reference, based on the assumption that vertical wind velocities are negligible (Chanin et al., 1989; Souprayen et al., 1999). The Doppler lidar uses a Nd:YAG laser operating at 532 ~~nm~~ nm in monomode. The pulse repetition rate of the laser is 30 ~~Hz~~ Hz with 24 ~~W~~ W mean energy. The 0.3 ~~m2~~ m^2 telescope of Maido wind lidar is composed of a single rotating mirror, which serves for both the emission and reception. The initial Rayleigh-Mie-Doppler wind profiles are retrieved with a temporal resolution of 5 minutes and a vertical resolution of 200 meters (Khaykin et al., 2016, 2018).

The present study uses individual lidar temperature and wind profiles of 15 min integration time and ~~150 m vertical resolution , along with lidar wind profiles of 5 min integration and 200 m vertical resolution~~ resampled to a vertical resolution of 100 m to characterize GWs with vertical wavelengths and observed periods > 1 km and 1 hour respectively. Lidar measurements are done during the 20 November 2023 night between 1543 UTC and 2028 UTC for temperature and between 1528 UTC and 2350 UTC for wind.

2.2 Gravity waves analysis techniques

2.2.1 The time averaged background profiles method

The nightly mean temperature profile is a simple, robust and widely used method for determining background temperature profiles (Gardner et al., 1989; Rauthe et al., 2008; Ehard et al., 2014). This approach assumes that the timescale of the background influencing temperature profiles is longer than the measurement period, while the timescale of GWs is relatively shorter ($\sim$3-12 hours). However, spectral bands of GWs are difficult to define. Alternatively, the background temperature profile can be determined using a running mean over a time window, typically around 3 hours (Yamashita et al., 2009). In this method, temperature variations with timescales longer than the window are attributed to the background profile and are excluded from the extracted GW spectrum. In our study, the nightly mean background temperature profile is derived by applying a Hanning window, with vertical smoothing performed using a 7.5 km vertical wavelength filter.

2.2.2 The sliding polynomial fit method

The ~~background temperature profilecan also be separated by fitting an nth-degree polynomial to the temperature profile, representing the background field (Allen and Vincent, 1995). The polynomial order is determined based on the height range of the analysis. If~~ Savitzky–Golay method, which consists of performing a local cubic polynomial regression on a sliding window of the vertical profile. The polynomial order and the window size are selected according to the vertical resolution of the measurements, making the method equivalent to applying a low-pass finite-impulse-response (FIR) filter with a well-defined frequency (wavelength) response. The height range L of the sliding window and the polynomial order determine the vertical wavelengths that are considered part of the background. Guest et al. (2000) reported that when L is the ~~total height range~~window size, a 2nd-order polynomial fit ~~removes perturbations with~~ may remove perturbations with vertical wavelengths greater than 2L~~. Similarly, 3rd and 4th-order polynomial fits can remove perturbations~~ , while a 3rd-order fit may remove those with wavelengths greater than ~~L~~L. Conversely, fits with order higher than 4 may also attenuate inertia–gravity wave signals and ~~$\frac{2L}{3}$, respectively. Polynomial fits of order greater than four may remove substantial GW signals from the analysis (Guest et al., 2000). To calculate the GW spectrum for use in numerical models based on radiosonde observations in the lower atmosphere of the Southern Hemisphere, Pfenninger et al. (1999) used different-order polynomials for different atmospheric layers. They applied lower-order polynomials (2nd or 3rd) for the troposphere, where the mean temperature profiles are mostly linear, and higher-order polynomials (above 3) for the stratosphere, where the mean temperature profiles are much more complex~~should therefore be avoided (Guest et al., 2000).

In our study, ~~the background temperature profile is determined using a 4th-order polynomialfit (with $\lambda_v < \frac{2L}{3}$. In this case~~we use a window width of 10 km and we fit the subdata to a third order polynomial. Hence, perturbations with vertical ~~wavelengths greater than 26 are removed from lidar perturbations profiles~~wavelength greater than 10 km are removed and associated with the background.

2.2.3 The spectral filtering method

Spectral filtering is another common method to study GWs. Contributions of GWs can be separated from the large scale waves by applying a high/low-pass filter of any cutoff wavelength. Generally, in order to remove low frequency components (or large scale waves) such as tides, high-pass filters are used in the time domain (or height domain) (Hirota, 1984; Hirota and Niki, 1985; Eckermann et al., 1995).

To isolate GW-induced perturbations specifically, the filtering function must be carefully selected to ensure an appropriate spectral response. Chane-Ming et al. (2000) applied a high-pass butterworth filter, with a cutoff of 12 km vertical wavelength, on individual temperature profiles to extract GW perturbations. They, hence, limit the vertical wavelength space to a GW field with vertical wavelengths < 12 km. The Butterworth filter is well adapted for the study of GWs due to its flat frequency response in the passband and is minimizing distortions while effectively isolating the desired wave components.

In this study, we apply a 5th-order Butterworth high-pass filter (Ehard et al., 2015) with a cutoff wavelength of 8 km, allowing us to extract GWs with the observed dominant vertical wavelength of 5 km during the studied night.

2.2.4 The variance method

The variance method, described by Mzé et al. (2014), is a technique used for calculating directly the potential energy density of GWs by using raw lidar signal, and is robust against data processing errors (Hauchecorne et al., 1994; Khaykin et al., 2015). The signal originates from an incoherent backscatter lidar operating in photon-counting mode. The raw signal is aggregated over small time and vertical intervals, allowing the vertical profile to be decomposed into a smooth mean profile (background signal) and short-scale perturbations. The relative perturbations, defined as $S'(z_i, t_j) = \frac{dS}{S}$, may arise from either instrumental noise or atmospheric fluctuations (where z_i and t_j are a given altitude and time, respectively) . To compute the observed variance and instrumental variance, larger time and ~~verticalsinterval~~ vertical intervals $(\Delta T, \Delta Z)$ are considered by grouping multiple elementary intervals such as $\Delta T = \Delta t N_t$ and $\Delta Z = \Delta z N_z$. The observed variance represents the sum of both instrumental and atmospheric variances and is defined as :

$$V_{obs} = \frac{1}{N_t N_z} \sum_{N_z} \sum_{N_t} S'(z_i, t_j)^2 \tag{1}$$

Since the lidar signal in photon-counting mode follows Poisson's distribution, the instrumental variance can be directly derived from the estimated mean signal S, except in cases of signal saturation due to exceptionally strong returns. The atmospheric variance is then obtained as the difference between the observed and instrumental variances :

$$V_{atm} = V_{obs} - V_{inst} \tag{2}$$

This atmospheric variance serves as an estimator of GW activity in the middle atmosphere and is used in the equation of ~~GW potential energy density (Wilson et al. 1991)~~ GWPE (Wilson et al., 1991) as followed:

$$E_p = \frac{1}{2} \left(\frac{g}{N}\right)^2 V_{atm} \tag{3}$$

Where V_{atm} is the equivalent of ~~$< \rho'/\rho_0 >^2$, hence $< T'/To >^2$~~ $(\rho'/\rho_0)^2$, hence $(T'/To)^2$ in adiabatic and linear conditions.

2.2.5 The multiresolution analysis method

This study focuses on the ~~MRA~~ multi-resolution analysis (MRA) based method of which the description of this new method is detailed as opposed to the four previous methods. The ~~multi-resolution analysis (MRA)~~ MRA framework provides the theoretical foundation for the discrete wavelet transform (DWT), enabling the hierarchical decomposition of a signal into different scales of approximation and detail. It decomposes a signal into orthonormal bases, capturing both coarse approximations

Table 1. ~~Filter bank for 8th order Daubechies wavelet (dark blue : d_1, orange : d_2, yellow : d_3, purple : d_4, green : d_5, lightblue~~ Vertical passbands from the different methods presented in this paper : ~~d_6~~(A) Nighttime average, ~~brown : a_6~~(B) Sliding polynomial fit, ~~Filter response for the variance method for $N_z = 21$ which represent the number of elementary altitude intervals~~ (~~black curve~~C) Spectral Filtering, ~~Butterworth low pass filter with a 8-km wavelength cutoff~~ (~~Dotted black curve~~D) Variance based method and (E) MRA.

~~Figure~~

Period (h)	> 1 ~~visualizes the spectral responses of the MRA using an 8th-order Daubechies wavelet with a six-level decomposition,~~
Vertical Wavelength (km)	

and successive details across multiple resolution levels. By adding or removing details, MRA enables a smooth transition between high and low resolutions, with each detail level encoding the differences in information between successive scales. The effectiveness of this approach is further enhanced by its flexibility in constructing orthogonal or biorthogonal bases tailored to the analyzed signal. When combined with efficient algorithms from subband coding theory and filter banks, MRA becomes a robust and adaptive tool for signal analysis (Mallat, 1989; Hubbard, 1998). The original signal is decomposed into successive octave bands (in the dyadic MRA, most widely used), with each level represented by an approximation of order n and discrete details up to that order, forming a pyramid-like wavelet decomposition tree, as described by Mallat's algorithm. Hence, the original signal can be decomposed as followed :

$$s(n) = d_1(n) + d_2(n) + d_3(n) + \cdots + d_i(n) + a_i(n) \tag{4}$$

The vertical resolution is crucial in this process, as adjusting it modifies the octave band limits, thereby altering the vertical wavelength bands. This adaptability allows for the selective extraction and analysis of GWs at different scales, depending on the chosen vertical resolution. Our method uses the orthogonal Daubechies wavelet which is mostly used in signal reconstruction. This wavelet and its corresponding scaling function of order 8 are sufficiently smooth to provide an optimal balance between computational efficiency and the quality of the decomposed ~~GW~~ multiscale signals (Chane-Ming et al., 2000; Chane Ming et al., 2023). All lidar profiles are oversampled to a vertical resolution of 100 m, however the study focuses on GWs with vertical wavelengths of 0.8-12.8 km. The 100 m vertical sampling provides different spectral domains corresponding to the wavelength bands : 0.2-0.4 km, 0.4-0.8 km, 0.8-1.6 km, 1.6-3.2 km, 3.2-6.4 km, 6.4-12.8 km and >12.8 km~~as shown in Fig. ??~~.

Table 1 ~~. By adjusting the vertical sampling, MRA offers additional control over filter responses, allowing for tunable selectivity.~~ summarizes the vertical and temporal passbands associated with the five filtering techniques used in this study. Since the filters are applied only along the vertical dimension of the lidar profiles, no temporal filtering is performed; therefore, wave periods longer than 1 h can be retrieved from the measurements as said in section 2.1. The vertical cutoff wavelengths are selected to be as consistent as possible across methods, allowing for a meaningful comparison of their spectral responses. The different approaches exhibit distinct vertical passbands. The nighttime average (A), polynomial fit (B), and spectral filtering (C) methods remove large-scale variations with cutoff wavelengths between 7.5 and 10 km, effectively isolating shorter vertical wavelengths. The variance-based method (D) targets a narrower band (2.5–6 km), reflecting its inherent design to isolate fluctuations within a defined vertical scale range. In contrast, the MRA (E) selects vertical bands between 1.6 and 6.4 km which corresponds to details d_4 and d_5 of the decomposition. These different passbands are used to characterize a dominant GWs, with a vertical wavelength of 5 km, propagating through the middle atmosphere.

~~GW potential and kinetic energy densities (~~GWPE and GWKE (Gravity Wave Kinetic Energy), in J.kg^{-1} ~~)~~ can be computed from the formulas given in ~~Wilson et al. (1991)~~ Wilson et al. (1991) :

$$E_p = \frac{1}{2}\left(\frac{g}{N}\right)^2 \overline{\left(\frac{T'}{T_0}\right)^2} \tag{5}$$

$$E_k = \frac{1}{2}\overline{u'^2 + v'^2} \tag{6}$$

Where g is the Earth acceleration, N the buoyancy frequency, T_0 the background temperature profile, T', u' and v' are, respectively, temperature, zonal wind, and meridional wind perturbations (~~w'~~ the vertical wind is neglected). The overline represents the average over the night of measurements.

The first step for computing ~~GW energy densities~~ GWPE and GWKE (Gravity Wave Kinetic Energy) is to determine the impact of the Gaussian white noise, present in the temperature and wind profiles, on the MRA decomposition. To do so, we ~~simulated~~ simulate temperature profiles with gaussian white noise $\mathcal{N}(0,1)$ and ~~computed~~ compute the potential energy of the gaussian white noise. A noise amplitude increasing with the altitude by a factor of $e^{\frac{z}{H}}$, where z is the altitude taken from 20 km to 80 km and H is the height scale (8 km), is here considered. Then, the mean energy is calculated on height intervals of 10 km for each detail from the MRA decomposition (level 6) of the 1000 gaussian white noise simulated signals to estimate the impact of the noise on the different spectral bands (Fig. 1).

~~The potential energy density of the noise is divided by 2~~ Before analyzing the noise contribution across the MRA levels, the data were oversampled to a 100 m vertical resolution. The original temperature profiles from lidar measurements have a vertical resolution of 150 m, which allows the detection of gravity waves with minimum vertical wavelengths of approximately 300 m. After oversampling, the first detail level of the MRA corresponds to vertical wavelengths between roughly 200 and 400 m. This interval contains only white noise, as GWs with vertical wavelengths shorter than 300 m cannot be resolved by the instrument.

Although white noise is present at all scales, the dyadic nature of the MRA leads to a progressive reduction of noise energy by a factor of 2^{n-1} at the n^{th} decomposition level. This behavior is illustrated in Fig. 1, where the normalized noise energy decreases by a factor of two at each step of the decomposition~~which is a~~, under the assumption that the first detail level d_1 contains only noise and it is direct consequence of the pyramidal decomposition of the MRA. Consequently, the noise-induced potential energy density calculated from d_n, E_{p_n}, can be estimated using an empirical formula, assuming that the first detail level of the MRA decomposition (E_{p_1}) consists solely of noise : ~~$E_{p_n} = \frac{E_{p_1}}{2^{n-1}}$~~ $E_{p_n} = \frac{E_{p_{noise}}}{2^{n-1}}$, with n varies from 2 to 6 for a decomposition at order ~~6.~~ 6, and $E_{p_{noise}}$ is the equivalent of computing E_{p_1}.

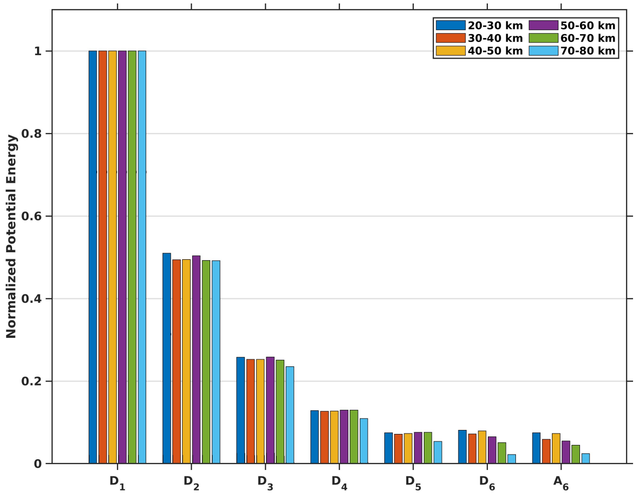

Figure 1. Normalized mean potential energy density of 1000 simulated Gaussian white noise signals for each detail level obtained from the MRA decomposition at heights between 20 and 30 ~~km~~ km (blue), 30 and 40 km (orange), 40 and 50 km (yellow), 50 and 60 km (purple), 60 and 70 km (green), 70 and 80 km (cyan).

The GW energy ~~density (GWED~~(potential or kinetic) is computed for each perturbation (temperature or wind) profile of the considered night of measurements. In order to subtract noise, we remove noise energy corresponding to the ~~nth~~ n^{th} detail treated by applying the empirical formula. Then, the nightly mean profile of the ~~GWE~~ GW energy is determined, and the mean profile is smoothed using a 7.5 km Hanning window. This process enables an estimation of the primary propagation characteristics of GWs observed during the night. With the MRA decomposition, it is possible to derive an energy profile that focuses on a dominant or quasi-monochromatic mode of ~~gravity waves~~Gws. It enables to highlight the ~~interaction between modes of GWs during the night~~evolution of GW modes and the interaction between them. Due to potential edge effects, the MRA method may bias GW energy ~~densities~~ density as it approaches the upper or lower limits of vertical profiles, depending on the order of the detail and the amplitudes of the signal. To mitigate edge effects, it is recommended to either reduce the vertical range of the ~~analyzed signal (e.g., analyzing the 30–70 range instead of the full 20–80 profile) or to apply signal symmetrization by extending the profile with a mirrored version of itself at both ends~~decomposed signal for further analysis.

3 Comparison of the different methods

In the following section, we demonstrate the capability of the MRA method to estimate both background ~~temperature~~ and perturbation profiles by comparing its results with those obtained from conventional ~~methods~~approaches, including time-averaging, polynomial fitting, and spectral filtering. ~~We further compare the GW potential energy derived from these four approaches with that obtained~~ First, the four methods are applied to the temperature profiles to extract background fields and wave-induced perturbations. The resulting GWPE estimates are then compared with those derived using the variance

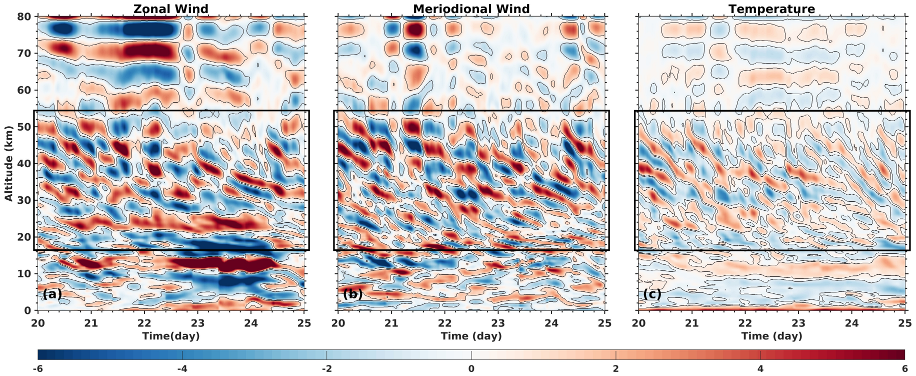

Figure 2. ~~Horizontal Zonal Wind~~ Height-time representation of (~~m/s~~a) ~~at 200 hPa~~ zonal wind (~~13~~ m.s^{-1})~~on 20 November 2023 at 1800 UTC derived from ERA 5 reanalysis (Hersbach et al., 2020)~~, (b) meridional wind (m.s^{-1}) and (c) temperature (K) perturbations above La Réunion (21.0°S,~~55,5~~55.5°E) ~~.~~ derived from ERA 5 reanalysis (Hersbach et al., 2020) from 20 November 2023 to 25 November 2023. The ~~subtropical jet is split into two main flows: one branch at latitudes~~ enhancement of ~~30°S and~~ perturbations, especially in the ~~second one at latitudes between 10°S and 15°S. A jet core with wind intensity~~ lower stratosphere, might be attributed to the presence of ~~30-40 m/s is visualized~~ the subtropical jet above La Réunion (~~21~~21.0°S,55.5°E). ERA 5 confirms the presence of gravity waves structures which can be seen in all perturbations plots (black boxes).

method ~~described by Mzé et al. (2014) , in order to evaluate their relative effectiveness. Lastly, we apply the MRA method to wind profiles~~of Mzé et al. (2014) to ~~investigate additional GW propagation characteristics~~ assess their relative performance. The same analysis is subsequently carried out using wind profiles, allowing for a direct comparison of the methods across both datasets. Finally, the ratio between GW kinetic and potential energy is calculated to provide additional insight into GW characteristics during the night. An illustrative case study is presented below.

3.1 Case study: 20th November 2023

The ~~GW energy densities~~ GWPE and GWKE derived from the MRA and conventional methods are illustrated using lidar profiles from the night of 20 November 2023. During this period, a split jet stream system was ~~observed~~ present between 30°S and 10°S (Homeyer and Bowman, 2013), ~~giving rise to instabilities and~~ generating instabilities and vertical wind shear that ~~contributed to pronounced~~ enhanced GW activity in both the troposphere and stratosphere over La Réunion. This episode occurred during the late austral winter (20–24 November 2023), and ERA5 reanalysis data reveal a ~~marked intensification of westerly winds over the island, associated with the passage of the upper-level jet stream~~ strong GWs activity clearly visible in zonal wind, meridional wind and stratospheric temperature perturbations over La Réunion (Fig. 2). ~~In addition, prominent 24-hour tidal signatures were detected in the zonal and meridional wind components above 30 , highlighting the presence of diurnal tidal waves in the upper stratosphere.~~

Vertical profiles of horizontal wind from ERA5 reanalysis (Hersbach et al., 2020) and radiosonde measurements on 20 November 2023 at 1200 UTC show good agreement and reveal the presence of short-scale GW structures (not shown). In particular, ERA5 wind profiles display clear stratospheric GW perturbations (boxes on Fig. 2a and b) with an estimated vertical wavelength of approximately 5 km during the night of November 20, ~~2023.~~ 2023 (Fig. 2). To further characterize these features, a hodograph analysis was performed by examining the altitude-dependent evolution of the horizontal wind components. It reveals ~~an~~ a GW elliptical structure at heights of 30-35 km ~~which characterizes a GW~~ with a vertical wavelength of 5 km. The counter-clockwise rotation of the ~~perturbation wind vector~~ ellipse with height indicates upward energy propagation into the middle stratosphere. The axis ratio of the ellipse provides an intrinsic wave period of about 23 h. Assuming that the dominant GWs propagate primarily in the vertical direction and are detectable at higher altitudes in the lidar profiles, the following sections focus on a detailed characterization of these wave structures.

3.2 Application to lidar temperature profiles

First, the MRA method is evaluated against conventional approaches by comparing the estimation of background temperature, temperature perturbations, and ~~GW potential energy density~~GWPE, using lidar temperature measurements acquired on 20 November 2023 between 1543 UTC and 2028 UTC, during ~~a~~ an approximately 5 hours observation period. Background temperature profiles were derived using spectral filtering with ~~butterworth filter with~~ cutoff wavelength at 8 km, ~~polynomial fitting with 4th~~ sliding polynomial fit with 3^{rd} order polynomial function, nighttime averaging over the 5 hours of measurement, and the MRA method, applied to lidar temperature measurements from the night of 20 November (Fig. 3~~).~~ a). In order to isolate GWs with dominant vertical wavelengths around 5 km within the MRA framework, we use the details d_4 (1.6-3.2 km) and d_5 (3.2-6.4 km), of which the sum effectively captures the wave structure. Between 30 and 45 km altitude, ~~all background estimates show similar values~~the background fields are consistent with each other, except for the ERA 5 temperature profile, which shows a warm bias of about 10 K near 30 km, decreasing progressively with altitude up to 45 km. However, near the stratopause, the ~~backgrounds~~ background obtained using nighttime averaging ~~and polynomial fitting are~~ is approximately 10 K lower than those produced by MRA~~and Butterworth filtering .~~, spectral filtering and sliding polynomial fit. In contrast, MRA, spectral filtering and sliding polynomial fit methods display consistent and smoother behavior, yielding a more realistic background structure at the stratopause level. The ERA5 temperature profile exhibits a stratopause altitude slightly lower than that observed in the raw lidar measurements. Above 50 km, the background derived from nighttime averaging begins to show noise-induced features unrelated to GWs ~~. In contrast, both the MRA and Butterworth filtering methods display consistent and smoother behavior, yielding a more realistic background structure~~ and the ERA5 temperature profile remains nearly constant, showing no apparent small-scale variability. By examining the temperature perturbations (Fig. 3b) obtained by subtracting the background from the original temperature profiles, it is evident that the perturbations derived using the MRA are smoother than those obtained from the conventional methods. Below the stratopause, the perturbation amplitudes are of the same order of magnitude across all methods. However, at the stratopause level, the perturbations obtained using the nighttime average method are almost twice as large as those from the other three methods. The MRA-derived perturbations are less noisy, particularly above 50 km, where GW amplitudes retrieved with conventional techniques can be up to twice as large as those derived with the MRA.

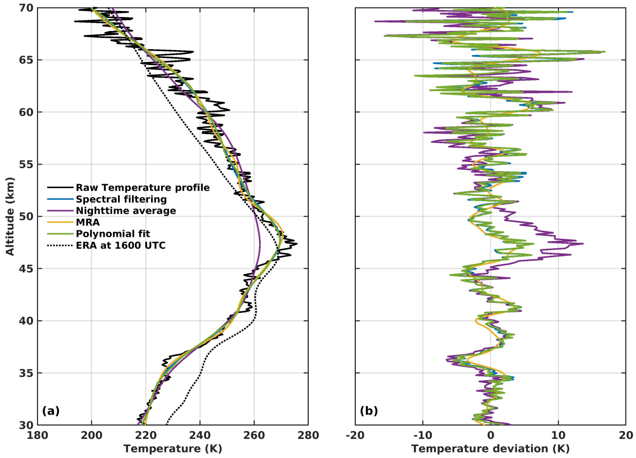

Figure 3. (Original temperature profile at 1543 UTC (black), background temperature retrieved by different methods (a) : ~~Butterworth filter~~ Spectral filtering (blue), ~~night mean profile~~ Nighttime average (purple), trend (~~a_6~~$d_6 + a_6$) obtained from the MRA (yellow) and ~~4th~~ 3^{rd} order sliding polynomial (green). The ~~approximation a_6~~ MRA trend corresponds to vertical wavelengths greater than ~~12.8~~ 6.4 km~~which are not considered as GWs~~.

~~Based on the hodograph analysis, we focus on GWs with dominant vertical wavelengths around 5 . To isolate these scales within the MRA framework, we use detail levels d_4 (1.6-3.2) and d_5 (3.2-6.4), which are suitable for capturing this wave structure. Perturbations extracted using different background removal methodsreveal~~ Figure 4 represents the temperature perturbations obtained from all the methods with respect to time and altitude. Across all methods, a distinct wave structure is visible at altitudes between 35 km and 45 km. This structure with a downward phase propagation (upward energy propagation) ~~with~~ is a typical GWs structure and has a vertical wavelength of approximately 5 km ~~at altitudes between 35 and 45~~ (Fig. 4). This feature appears more pronounced in the ~~Butterworth-filtered temperature perturbations and the MRA-derived~~ spectral filtering, the MRA and sliding polynomial derived signals, highlighting the consistency of the MRA approach with conventional ~~spectral filtering~~ techniques. Above the stratopause (~~51~~ 47.5 km), ~~the Butterworth method emphasizes smaller-scale perturbations compared to MRA. In contrast, the night-mean and~~ waves structures are less visible in height time representation for nighttime average, spectral filtering and sliding polynomial fit methods ~~produce~~ mainly due to a decrease in signal to noise ratio. Moreover, the nighttime average method produces incoherent perturbation values at these heights~~(Figs. 4c, 4d)~~. The MRA effectively reveals the 5-km vertical wavelength structure, which is clearly visible in the extracted perturbations. The results closely match those obtained using other background removal methods, particularly the ~~Butterworth filter~~spectral filtering and sliding polynomial fit, which also ~~highlights~~ highlight this wave component. However, the MRA is less sensitive to noise, resulting in improved signal clarity and a higher signal-to-noise ratio. These advantages underscore the effectiveness of the MRA in detecting GWs at this scale, making it a robust and reliable alternative to conventional filtering techniques.

The main ~~part~~ focus of the study is the computation of ~~the GW potential energy of which~~ GWPE, using the variance method ~~is taken~~ (Mzé et al., 2014) as a reference ~~(Mzé et al., 2014). The GW potential energy density from the variance~~

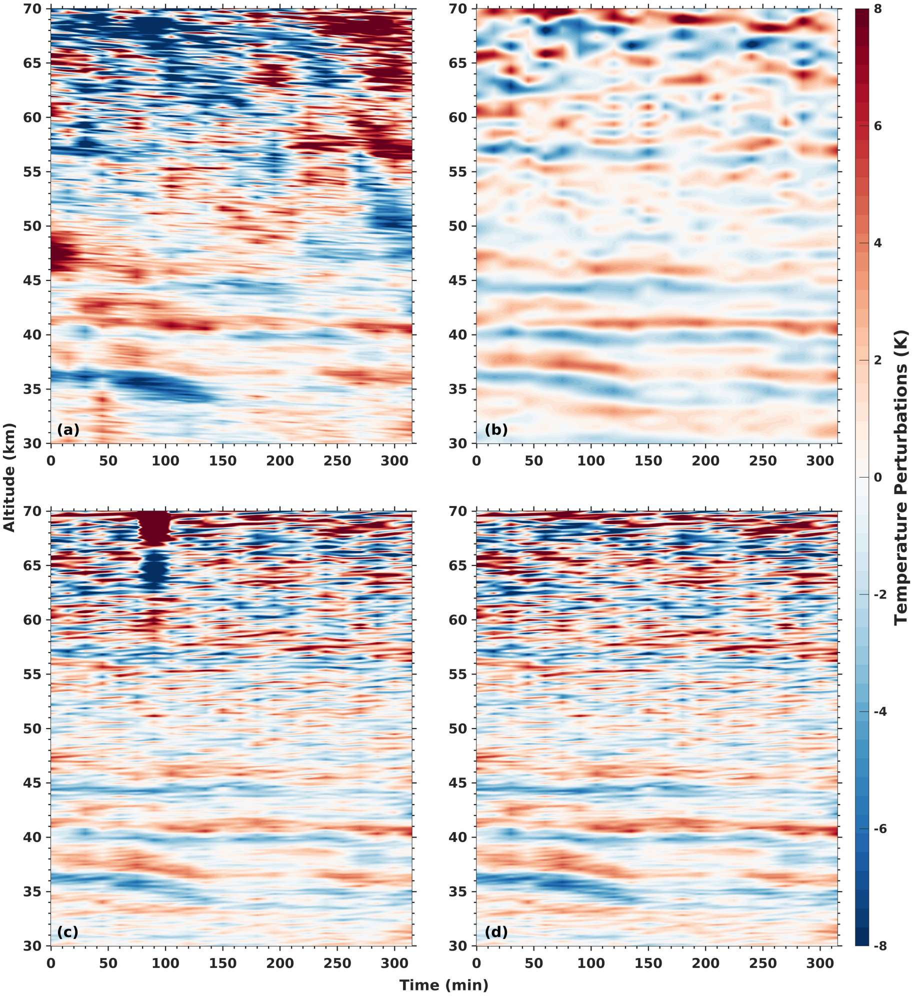

Figure 4. Height-time distribution of the temperature perturbations for the 20^{th} November 2023 night obtained from the four methods: nighttime average (a), MRA focused on d_4 (1.6 - 3.2 km) and d_5 (3.2 - 6.4 km) (~~a~~b), ~~Butterworth~~ Spectral filter with a cutoff wavelength of 8 km (~~b), night mean (~~c), ~~4th order~~ sliding polynomial fit with 3^{rd} order polynomial (d)

~~method computed for GW with~~ in terms of both vertical trends and values. To assess the effectiveness of the MRA approach, we compute the absolute differences in GWPE between the MRA and the other methods. In this part of the analysis, the GWPE is evaluated for GWs with a vertical wavelength of 5 ~~vertical wavelength is taken as a reference~~km across all methods. Vertical profiles of ~~GW potential energy density~~ GWPE derived from the MRA (~~focus~~ focusing on details d_4 and d_5), ~~Butterworth filtering, night-mean, and polynomial fit methods exhibit similar trends up to 50-km height~~ spectral filtering, nighttime averaging, and sliding polynomial fitting exhibit similar vertical behaviors to those obtained with the variance method up to approximately 45 km altitude (Fig. 5).

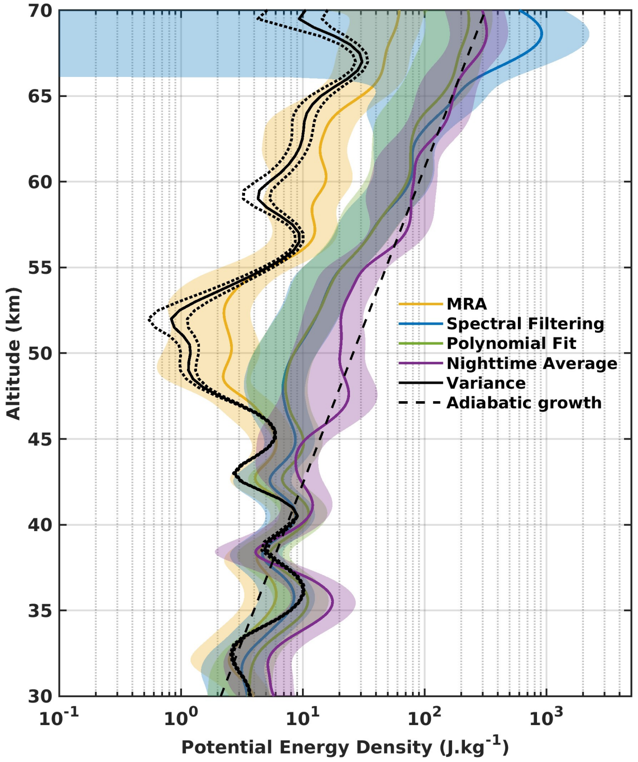

Figure 5. Mean ~~GW potential energy density~~ GWPE on the night of 20 November 2023, derived using different methods: variance method (black), MRA (yellow), ~~Butterworth~~ spectral filter with an 8 km cutoff (blue), night-mean subtraction (purple), and polynomial fit (green). Dotted black lines represent the variance method error, dashed line represent the adiabatic growth, and shaded areas indicate the 95 % confidence intervals.

~~Although the variance method profile follows the same overall trend, it exhibits an altitude shift. This offset arises because the variance method computes energy density directly from the raw lidar signal, whereas the other four methods rely on temperature profiles that require additional assumptions during retrieval. Furthermore, since the raw signal is proportional to atmospheric density, a phase shift develops between temperature and density caused by the hydrostatic integration of the pressure profile from the bottom upward. This phase shift becomes more pronounced for GWs with longer vertical wavelengths. While the altitude shift can be determined for simulated monochromatic waves, it is more challenging to quantify when analyzing a full spectrum of GWs.~~ In addition, the ~~night-mean and polynomial fit profiles yield~~nighttime average profile yields, on average, potential energy values roughly twice as large as those derived from the MRA ~~. Above 50~~ below the height of 45 km . Above 45 km altitude, the potential energy density profiles begin to diverge: whereas the MRA and ~~Butterworth~~ spectral filtering methods show a decrease in ~~GW potential energy density~~GWPE, the night-mean and polynomial fit methods instead exhibit an increase. At 55-km height, the GWPE derived from MRA reaches its minimum, indicating GW breaking or filtering at this altitude. The ~~Butterworth~~ spectral filtering method also detects this minimum, but at slightly lower heights and with GWPE

Table 2. Relative error (in %) of GWPE and GWKE (in parentheses) for the different methods, with MRA-derived values (from d_4 and d_5) taken as the reference. Deviations are computed over different altitude ranges from 10 km to 70 km. A hyphen indicates that the corresponding value is not available.

Altitude Range (km)	10 - 20	20 - 30	30 - 40	40 - 50	50 - 60	60 - 70
Variance	- (-)	- (-)	23.81 (-)	12.55 (-)	41.15 (-)	55.03 (-)
Spectral filtering	- (63.57)	- (30.05)	23.30 (92.12)	56.24 (55.14)	304.94 (42.24)	892.28 (-)
Sliding polynomial	- (114.84)	- (37.92)	50.48 (95.96)	79.40 (75.24)	299.03 (58.75)	328.30 (-)
Nighttime average	- (21.25)	- (91.40)	97.46 (634.00)	209.98 (1.94×10^3)	520.12 (2.42×10^3)	477.54 (-)

values three to four times higher. In contrast, the night-mean and polynomial fit methods do not capture the minimum and instead yield GWPE values ten times higher than those from MRA. Above 60-km height, the three conventional methods exhibit similar trends, with energy density values exceeding the expected density decrease, highlighting the impact of noise on the energy density profiles. Meanwhile, the MRA-derived GWPE profile closely follows the decreasing density curve.

~~Disregarding the altitudeshift,~~ At heights between 30 km and 70 km altitude, GWPE values from the MRA method ~~produces GW potential energy density values that are generally comparable to those obtained~~ agree with the variance method ~~between~~ to within a relative error of approximately 30 ~~and 70 altitude.~~ %.

The GWPE profile derived from the MRA also mirrors the overall trends observed with the variance method: an increase between 30 km and 40 km, followed by a decrease to a minimum around ~~52.5~~ 50 km, and then a ~~renewed rise above 55~~ rise above 52.5 km, consistent with the expected exponential growth linked to the decrease in atmospheric density. Notably, near ~~55~~ 50 km altitude, the MRA energy density profile shows values approximately ~~twice as high as~~ 30 % higher than those of the variance method (Table 2); however, the variance method's estimates remain within the MRA's 95 % confidence interval. ~~Overall, despite the observed altitudeshift~~Between 30 and 40 km, spectral filtering, sliding polynomial fit and nighttime average methods have values 23 %, 50 % and 97 % higher respectively to those derived from MRA. This relative error is increasing with respect to altitude, corresponding to the decrease of the signal to noise ratio mentionned previously. Hence, the noise has a strong impact on GWPE derived from conventional methods. Overall, the MRA demonstrates strong agreement with the variance method, highlighting its reliability in estimating GWPE. The noise handling in the MRA method allows for a more accurate estimation of GWPE, particularly in the mesosphere.

3.3 ~~Application to lidar wind profiles~~

3.3 Application to lidar wind profiles

Wind measurements obtained from lidar rely on ~~calculating~~ determining the phase shift of the Doppler signal. As a result, it is not possible to apply a variance-based method to ~~derive~~ directly estimate kinetic energy density ~~directly~~ from wind lidar data.

~~The earlier results have shown~~ Previous results have demonstrated the effectiveness of the MRA approach for analyzing GWs. Applying the MRA to wind lidar profiles successfully isolates perturbations with a vertical wavelength of around 5 km from detail coefficients d_4 and d_5. ~~This wave~~

At heights between 7 to 30 km, the GW pattern is clearly visible ~~from the surface up to the highest observed altitudes in both zonal and meridional wind perturbations~~across all zonal wind perturbations, regardless of the method used (Fig. 6).

~~Height-time representation of zonal wind (a) and meridional wind (b) perturbations. Perturbations of wavelength ranging from 1.6 to 6.4 (d_4 and d_5) are represented in the height-time representation.~~

~~Figure **??**a vizualises zonal and meridional wind perturbations lidar profiles from MRA detail d_5 (λ_v = 3.2-6.4) on 20 November 2023. From 20 to 45 , observed GW amplitudes are decreasing for both zonal and meridional winds and are increasing above 45 . Phase quadrature is visible at altitudes between 51.1 and 54.9 , hence, a hodograph analysis confirms the presence of an elliptical GW pattern with a vertical wavelength of 5 at those altitudes~~ Between 7 and 15 km, gravity wave structures are visible in all perturbation fields derived from the different methods. However, amplitude enhancements in this altitude range are more pronounced for the spectral filtering and sliding polynomial fit methods (Fig. 6c, 6d), whereas the MRA and nighttime averaging methods (Fig. ~~**??**b) . Moreover, the orientation of the major axis suggests a horizontal propagation direction aligned north~~6a, 6b) exhibit less amplification. Above 30 km, small-scale perturbations not related to gravity waves appear in the results from the spectral filtering and sliding polynomial fit methods (Fig. 6c, 6d). In contrast, the MRA-derived perturbations still exhibit coherent GW signatures in this altitude range. The nighttime averaging method (Fig. 6a) shows limitations above 30 km height, where it struggles to properly estimate GW perturbations and background winds in the upper stratosphere~~–south, perpendicular to the jet orientation. The anticlockwise rotation of the hodograph indicates upward propagation of GW energy into the mesosphere. The length and axis ratio of the ellipse further yield an estimated vertical wavelength of 5 and an intrinsic period of around 23 hours~~lower mesosphere (30–60 km) region.

~~To go further in understanding the GW propagation, the kinetic energy density from the MRA for each detail can be computed. As an example, the MRA method is applied on the wind lidar profile, and the mean kinetic energy density is computed on~~ In the following results, we compare GWKE derived from the different methods. Nevertheless, we compute GWKE for the different details of MRA, corresponding to specific vertical wavelengths bands. Figure 7 represents the mean GWKE over the night of ~~20 November 2023 (Fig. 7)~~measurement for MRA d_2 to d_5 (d_6 is considered as background), spectral filtering, nighttime average and sliding polynomial methods.

~~At heights above~~ Between 10 and 15 km, ~~kinetic energy densities for~~ an enhancement of GWKE is observed across all methods. This increase is most pronounced for the smaller-scale gravity waves (details d_2, d_3, ~~d_4 and d_5 increase up to 35 , 50~~ and ~~25~~ d_4). Such an enhancement may be associated with the subtropical jet, which is known to generate small-scale gravity waves (Plougonven and Zhang, 2014). Conventional approaches do not explicitly separate contributions from different vertical wavelengths, so while the enhancement is still visible, it appears less amplified than in the MRA results. Above 15 km~~respectively in contrast with the kinetic energy density for detail d_6 showing a decrease up to 30~~, the GWKE associated with details d_2, d_3, and d_4 increases steadily up to 30-35 km~~. However, from 25 to 45~~. A similar increase is observed for the conventional methods, showing a coherent growth up to around 30 km, ~~kinetic energy density for~~ after which their

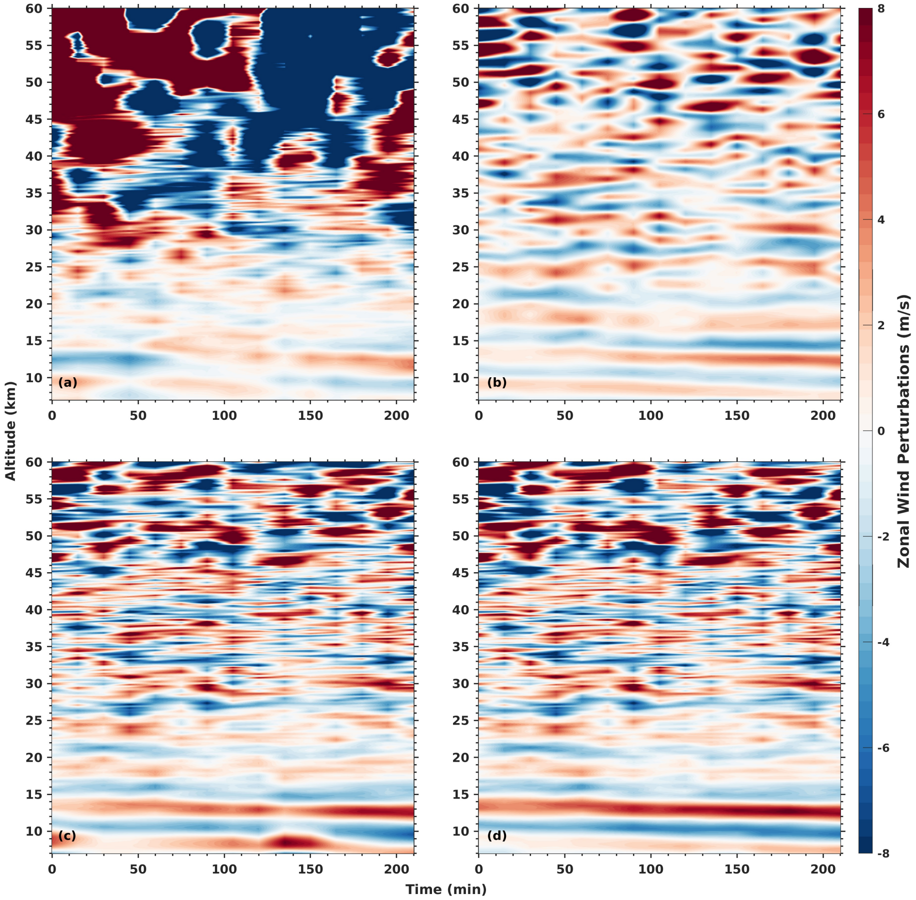

Figure 6. ~~Zonal and meridional~~ Height-time distribution of the zonal wind perturbations for the 20th November 2023 night obtained from the four methods: nighttime average (a)~~and hodograph analysis~~, MRA focused on d_4 (~~blue line~~1.6 - 3.2 km) ~~from 51.1 to 54.9~~ and d_5 (3.2 - 6.4 km) (b)~~on 20 November 2023; Blue and red dots indicate height interval~~, spectral filter with a cutoff wavelength of ~~100 m and starting point at 51.1~~ 8 km ~~respectively. Dotted black lines represent the elliptical~~ (c), sliding polynomial fit ~~function and major and minor axes obtained by the least mean square method.~~with 3rd order polynomial (d)

GWKE profiles begin to diverge. The GWKE derived from the nighttime average method continues to increase, whereas the spectral filtering and sliding polynomial fit methods show a slight decrease up to approximately 40 km. In contrast, the GWKE associated with detail d_5 ~~is decreasing. Nevertheless, kinetic energy densities for d_2 and d_3 ceases to increase at 35 corresponding to higher values of~~ decreases within this altitude range. Above 45 km, the GWKE for d_4, d_5, spectral filtering, and sliding polynomial fitting starts to increase again, while the kinetic energy for ~~d_6. A connection between GWs with wavelengths between~~ d_2 and d_3 continues to decrease. The MRA results also highlight a connection between gravity waves with vertical wavelengths of 0.4-1.6 km and 3.2-6.4 km~~and larger GWs with wavelengths between 6.4-12.8 is highlighted by the result of the MRA. Above 45~~, suggesting interactions between smaller- and larger-scale waves. Such interactions cannot

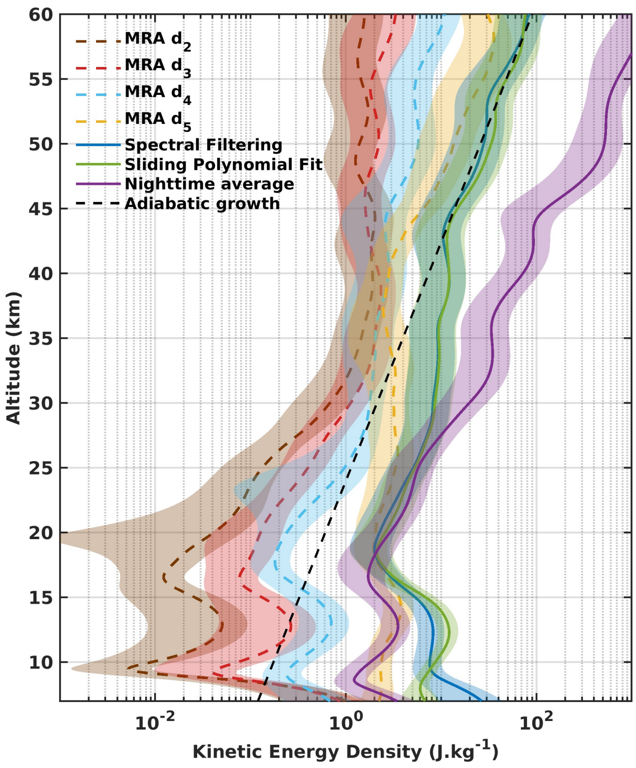

Figure 7. Mean ~~GW kinetic energy density (b) during~~ GWKE on the night of 20 November ~~2023. Energy densities are computed from perturbations extracted~~ 2023, derived using ~~MRA decomposition at~~ the different ~~scales~~methods: nighttime average method (purple), spectral filtering (blue), sliding polynomial fit (green), d_2 (0.4-0.8 km, ~~blue~~ brown), d_3 (0.8–1.6 km, ~~yellow~~red), d_4 (1.6–3.2 km, ~~purple~~light blue), d_5 (3.2–6.4 km, ~~green), and d_6 (6.4–12.8 , red~~yellow). Shaded areas indicate the 95 % confidence intervals.

be inferred from the conventional approaches, where the GWKE associated with smaller-scale gravity waves is mixed with that of the dominant 5 km ~~, kinetic energy for d_4, d_5~~ waves, preventing their separation. In terms of GWKE values, clear differences between the methods are observed depending on altitude. In the 10-20 km height range, GWKE obtained from spectral filtering, sliding polynomial fitting, and nighttime averaging methods are approximately 60 %, 115 %, and 20 % higher, respectively, than the GWKE derived from MRA details d_4 and ~~d_6 is increasing whereas the kinetic energy for d_2 and d_3 still decreasing~~d_5. Between 20 and 30 km, GWKE from spectral filtering and sliding polynomial fitting shows better agreement with MRA, with values about 30 % and 40 % higher, respectively. In contrast, GWKE derived from the nighttime averaging method is almost twice as large as that obtained from MRA (approximately 90 % higher). Above 30 km, the GWKE from the nighttime averaging method starts to diverge strongly, exceeding MRA-derived values by more than 600 %, with the overestimation continuing to grow into the lower mesosphere. In the same altitude range (30-40 km), spectral filtering and sliding polynomial fitting methods overestimate GWKE by about 90 %. Beyond this layer, the relative differences decrease to approximately 50 % for spectral filtering and 65 % for the sliding polynomial fit method.

The ratio of kinetic ~~energy density~~ to potential energy density (hereafter ER) was computed for three altitude intervals~~30-40~~ : 30–40 km, ~~40-50~~ 40–50 km, and ~~50-60~~ 50–60 km~~for each detail of the MRA decomposition~~ , using the different methods and the MRA detail coefficients d_2, d_3, d_4, and d_5 (Fig. 8). ~~For~~

Between 30 and 40 km, the ER exhibits similar values and temporal behavior for the spectral filtering, sliding polynomial fitting, and MRA methods. A pronounced minimum (ER ~ 1) is observed for MRA detail d_5. In contrast, the ER derived from the nighttime average method shows incoherent values compared to the other approaches, but gradually increases from about 100 minutes after the start of the measurements until the end of the night. Between 40 and 50 km, the ER derived from all methods shows comparable values (around 15-20) and similar temporal trends, except for the nighttime average method, which exhibits larger variability. Oscillations are observed in the ER for all methods. These oscillations may reflect the modulation of gravity wave activity by GWs with short periods (~ 1 h). Between 50 and 60 km, the ER values obtained from spectral filtering, sliding polynomial fitting, and nighttime averaging remain broadly similar, but are lower than those found in the stratopause region. In this lower mesosphere layer, the conventional approaches yield ER values close to 10. In contrast, the ER from MRA reaches values of around 100, indicating a predominance of kinetic over potential energy and revealing a different behavior for the dominant 5 km vertical wavelength GWs. The MRA results thus highlight a change in wave frequency as they propagate through the middle atmosphere.

For the MRA details d_2, d_3, ~~d_5, and d_6, this ratio increases~~ and d_4, the ER slightly decreases from 30-40 km to ~~40–50~~ 40-50 km, whereas ~~for detail d_4 it decreases~~ it increases for detail d_5 over the same altitude range. From 40-50 km to 50-60 km, the ~~ratio~~ ER decreases for the smaller vertical wavelengths (d_2~~and~~ , d_3), but increases for the larger vertical wavelengths (~~d_4,~~ d_5, ~~and d_6~~d_4). This evolution reflects the modification of the ~~GWs~~ GW frequency distribution with altitude (Wilson et al., 1990). ~~Between the stratosphere and lower mesosphere (approximately 40-60), low-frequency GWs are increasingly damped, leading to a decreasing energy ratio for these components at higher altitudes. In contrast, high-frequency GWs continue to propagate into the mesosphere, maintaining or increasing their energy ratio. Furthermore, the increase in the ratio for d_4, d_5, and d_6 with altitude can be interpreted as a shift in the nature of GWs. As low-frequency waves are filtered out in the lower mesosphere, the intrinsic frequency of the remaining GWs approaches the Coriolis frequency, suggesting that inertia-gravity waves become dominant in the mesosphere~~The increase in ER observed for detail d_5 suggests a transition toward lower-frequency gravity waves, where the kinetic energy component tends to dominate over the potential energy (Geller and Gong, 2010).

Overall, the MRA highlights features of GW propagation through the middle atmosphere that remain hidden when using conventional approaches. In particular, MRA brings to light interactions between different wave scales during propagation. A transfer of momentum from smaller- to larger-scale GWs may occur, potentially indicating the presence of secondary wave sources in the middle atmosphere.

4 Summary, conclusions and perspectives

This study ~~presented the implementation of a method based on the MRAperfomed~~ implemented a multiresolution analysis (MRA) with the 8~~^{t}h~~ th order Daubechies wavelet to investigate GWs ~~. The approach was evaluated by comparing results~~

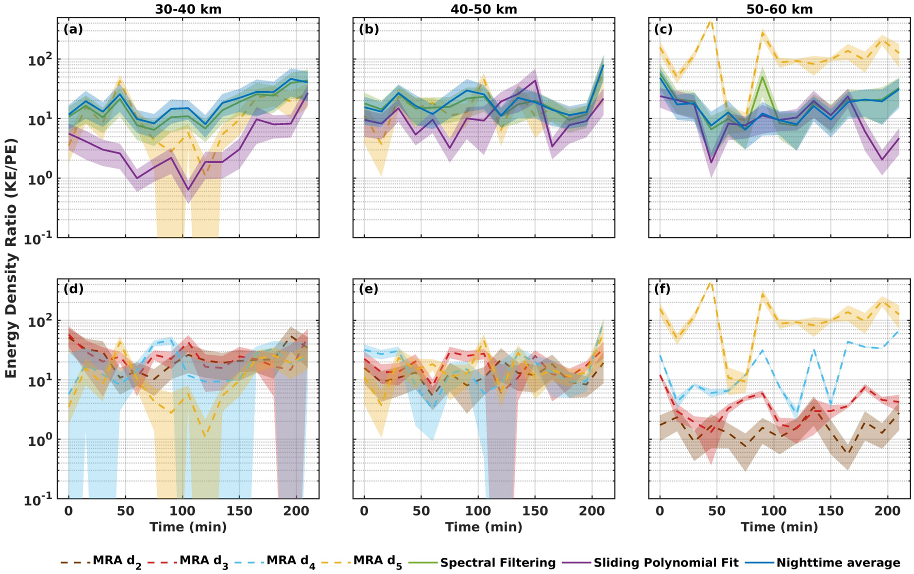

Figure 8. Energy ~~density~~ ratio (~~KE~~GWKE/~~PE~~GWPE) computed for nighttime average method (purple), spectral filtering (blue), sliding polynomial fit (green), MRA details d_2 (~~blue~~brown), d_3 (~~yellow~~red), d_4 (~~purple~~light blue), d_5 (~~green) and d_6 (red~~yellow) during the 20 November 2023 night between 30-40 km (a, d); 40-50 km (b, e) and 50-60 km (c, f). Shades represent the uncertainty error.

~~obtained from MRA with those from conventional methods, including night-mean subtraction,~~ from lidar observations at La Réunion. We compared MRA with three conventional background removal techniques-nighttime average subtraction, sliding polynomial fitting, and spectral filtering~~. The analysis is illustrated on a case study from~~ —and used the variance method (Mzé et al., 2014) as a reference for GWPE. A case study on 20 November 2023, ~~when a split jet structure, along with associated instabilities and wind shear, generated significant GW activity in the troposphere above La Réunion. The decompositionprovided by MRA enabled~~ during a split-jet episode, exhibited pronounced GW activity. ERA 5 reanalysis also shows coherent wind and temperature perturbations over La Réunion from 20th November to 25th, lending external support to the observed wave signatures.

The primary differences between the approaches arise from their distinct vertical spectral passbands, rather than from any intrinsic bias of a particular technique. The nighttime average method, widely used to estimate background temperature or wind by time averaging over the measurement period, is sensitive to all variability occurring on the timescale of the observations, including contributions from planetary waves and tides. Because the duration of nighttime measurements can vary substantially from one night to another, the portion of the gravity wave spectrum retained after background subtraction may likewise vary between nights. In our implementation, applying a 7.5 km Hanning window provides a consistent vertical cutoff, systematically filtering perturbations with vertical wavelengths > 7.5km.

The sliding polynomial fit method involves performing a local cubic polynomial regression on a sliding vertical window. The polynomial order and window size must be carefully selected according to the vertical resolution of the measurements, as these parameters determine the effective spectral response of the filter. Consequently, the method requires tuning whenever the vertical resolution of the data changes.

As an alternative, spectral filtering using a Butterworth filter offers a more straightforward and flexible approach. This technique is not dependent on the vertical resolution of the profile and allows easy adjustment to any desired cutoff wavelength, while remaining simple to implement.

Conceptually, MRA is equivalent to applying a bank of band-pass filters, but it offers several distinctive advantages. The choice of wavelet and vertical sampling determines the position and width of the dyadic bands, thereby controlling the amplitude response of each scale. Changing the wavelet affects the spectral response and can modify the retrieved GW amplitudes. For lidar applications, previous studies have shown that the Daubechies wavelet at order 8 is well adapted for the analysis of GW perturbation in the middle atmosphere (Chane-Ming et al., 2000), which motivated its use in this study.

Beyond this filtering analogy, a key strength of MRA lies in its orthonormal decomposition, which ensures that the total signal energy is exactly partitioned across the different scales. This property enables energy-conserving reconstruction of GW perturbations, providing a physically consistent way to examine wave energetics across scales—something that polynomial fits and standard spectral filters do not guarantee. Furthermore, MRA provides simultaneous spatial and spectral localization, allowing the tracking of GW structures ~~along individual lidar profiles. When~~ and their energy distribution as they evolve with altitude. This makes it particularly well suited for studying multi-scale interactions, such as energy transfer between wave components, which are difficult to isolate with conventional filtering techniques.

All approaches were applied to temperature ~~lidar measurements, MRA showed strong agreement with the Butterworth spectral filtering in estimating the background field. While the dominant structure of 5-km vertical wavelengthwas also visible in perturbations extracted by conventional methods, those methods proved~~ and wind lidar data with close vertical cutoff in order to identify the dominant GW structure with $\sim$5 km vertical wavelength. In our study, the different approaches consistently identify this dominant GW structure; however, their behavior diverges with increasing altitude and decreasing signal-to-noise ratio. Conventional methods are simple and effective in the lower stratosphere, but they are more susceptible to noise ~~. By~~ above $\sim$50 km, and mix contributions from different vertical wavelengths, which can bias energy estimates. In contrast, MRA ~~offered more precise space(in terms of altitude) and time (during the observation period) localizationand highlighted multiscale GW structures. Additionally, comparison of GW potential energy profiles derived from MRA and from~~ yields smoother perturbations at high altitudes, provides sharper vertical time localization, and produces multi-scale diagnostics within a single, coherent framework. GWPE from MRA agrees well with the variance method ~~underscored an altitude shift introduced by integrating density to retrieve temperature profiles which is dependent on the GWs vertical wavelength.~~ up to $\sim$45-50 km and follows the expected density scaling at higher levels, where conventional methods increasingly overestimate energy due to noise.

To deepen the understanding of GW propagation from their generation in the lower atmosphere to their dissipation and breaking in the middle atmosphere, MRA ~~enables the calculation of~~ provides a unique framework to calculate scale-resolved energy density profiles~~(both~~. Both kinetic and potential energy densities ~~)~~ can be estimated for each detail, corresponding to tunable vertical wavelength bands ~~with octave or~~ defined by the dyadic wavelet decomposition. ~~These energy density profiles~~

~~reveal~~ This approach yields a consistent and energy-conserving quantification of how GW energy ~~density~~ is distributed across scales~~, and~~.

In addition, computing the kinetic-to-potential energy ~~density ratio across different altitude ranges offers insights into~~ ratio within specific altitude ranges allows the characterization of the vertical evolution of ~~GW~~ wave frequency distribution and intrinsic ~~wave characteristics. The combined multi-scale energy density profiles from MRA also~~ properties. Such diagnostics provide insight into processes such as filtering, dissipation, and scale-dependent changes in wave energetics.

A further strength of the MRA is its ability to reveal interactions between ~~different GW~~ wave components of different scales, which ~~are harder to detect using other approaches.~~ remain largely hidden with conventional filtering techniques. This highlights its potential to capture momentum transfers and secondary wave generation processes, offering new perspectives on how gravity waves shape the dynamics of the middle atmosphere.

Looking ahead, statistical analyses and climatological studies of larger lidar datasets could be used to characterize GW propagation more systematically above La Réunion. Extending the study to include the troposphere, through the integration of radiosonde data or reanalysis outputs, could help identify GW properties linked to their specific sources such as tropical cyclones during austral summer. Since GW characteristics depend on their generation mechanisms and the way they interact as they propagate, this multi-scale perspective is especially valuable. ~~However, it is important to acknowledge the inherent limitations of lidar observations, which are primarily one-dimensional and mostly available during nighttime, limiting the reconstruction of horizontal wave structures and full 3D GW dynamics.~~ Future observational strategies should aim to combine lidar measurements with complementary instruments such as radiosondes, satellite sounders, or GNSS radio occultation profiles. Such multi-instrument synergy could provide a more complete and nuanced view of GW propagation and vertical energy transfer in the atmosphere.

. The multiresolution analysis implemented in this study was developed in MATLAB, relying on functions from the Wavelet Toolbox.

. The OPAR lidar data can be obtained through the NDACC database at https://ndacc.larc.nasa.gov/. The post-processed data used in this study are available upon request from the principal investigators: AH for the temperature lidar and SK for the wind lidar. ERA5 model-level reanalysis data were obtained from the Copernicus Climate Change Service (C3S) Climate Data Store using the CDS API. The dataset used is: "ERA5: Fifth generation of ECMWF atmospheric reanalyses of the global climate" (DOI: https://doi.org/10.24381/cds.143582cf). The data were generated by the European Centre for Medium-Range Weather Forecasts (ECMWF).

. ST, FCM conceived the study. AH and SK post-processed the temperature and wind lidar data respectively. Wind lidar measurements were conducted by SK and MR. FCM, AH and PK offered scientific insights. The paper was written by ST with contributions of all authors.

. The authors declare that they have no conflict of interest.

. The authors thank scientific and technical teams who contributed to the data acquisition at the Maïdo Observatory (https://www.osureunion.fr/). We acknowledge the use of ERA5 reanalysis model-level data provided by the Copernicus Climate Change Service (C3S), generated by ECMWF.

References

Achatz, U., Alexander, M. J., Becker, E., Chun, H.-Y., Dörnbrack, A., Holt, L., Plougonven, R., Polichtchouk, I., Sato, K., Sheshadri, A., Stephan, C. C., Van Niekerk, A., and Wright, C. J.: Atmospheric Gravity Waves: Processes and Parameterization, Journal of the Atmospheric Sciences, 81, 237–262, https://doi.org/10.1175/JAS-D-23-0210.1, 2024.

Alexander, S. P., Klekociuk, A. R., and Murphy, D. J.: Rayleigh lidar observations of gravity wave activity in the winter upper stratosphere and lower mesosphere above Davis, Antarctica (69°S, 78°E), Journal of Geophysical Research, 116, D13 109, https://doi.org/10.1029/2010JD015164, 2011.

Allen, S. J. and Vincent, R. A.: Gravity wave activity in the lower atmosphere: Seasonal and latitudinal variations, Journal of Geophysical Research: Atmospheres, 100, 1327–1350, https://doi.org/10.1029/94JD02688, 1995.

Andrews, D. G., Leovy, C. B., and Holton, J. R.: Middle Atmosphere Dynamics, vol. 40, ISBN 978-0-12-058576-2, 1987.

Baray, J.-L., Courcoux, Y., Keckhut, P., Portafaix, T., Tulet, P., Cammas, J.-P., Hauchecorne, A., Godin Beekmann, S., De Mazière, M., Hermans, C., Desmet, F., Sellegri, K., Colomb, A., Ramonet, M., Sciare, J., Vuillemin, C., Hoareau, C., Dionisi, D., Duflot, V., Vérèmes, H., Porteneuve, J., Gabarrot, F., Gaudo, T., Metzger, J.-M., Payen, G., Leclair De Bellevue, J., Barthe, C., Posny, F., Ricaud, P., Abchiche, A., and Delmas, R.: Maïdo observatory: a new high-altitude station facility at Reunion Island (21° S, 55° E) for long-term atmospheric remote sensing and in situ measurements, Atmospheric Measurement Techniques, 6, 2865–2877, https://doi.org/10.5194/amt-6-2865-2013, 2013.

Binder, M. and Dörnbrack, A.: Observing Gravity Waves Generated by Moving Sources With Ground-Based Rayleigh Lidars, Journal of Geophysical Research: Atmospheres, 129, e2023JD040 156, https://doi.org/10.1029/2023JD040156, 2024.

Brhian, A., Ridenti, M. A., Roberto, M., De Abreu, A. J., Abalde Guede, J. R., and De Campos, E.: A Survey on Gravity Waves in the Brazilian Sector Based on Radiosonde Measurements From 32 Aerodromes, Journal of Geophysical Research: Atmospheres, 129, e2023JD039 811, https://doi.org/10.1029/2023JD039811, 2024.

Bègue, N., Mbatha, N., Bencherif, H., Loua, R. T., Sivakumar, V., and Leblanc, T.: Statistical analysis of the mesospheric inversion layers over two symmetrical tropical sites: Réunion (20.8° S, 55.5° E) and Mauna Loa (19.5° N, 155.6° W), Annales Geophysicae, 35, 1177–1194, https://doi.org/10.5194/angeo-35-1177-2017, 2017.

Chane-Ming, F., Molinaro, F., Leveau, J., Keckhut, P., and Hauchecorne, A.: Analysis of gravity waves in the tropical middle atmosphere over La Reunion Island (21°S, 55°E) with lidar using wavelet techniques, Annales Geophysicae, 18, 485–498, https://doi.org/10.1007/s00585-000-0485-0, 2000.

Chane Ming, F., Hauchecorne, A., Bellisario, C., Simoneau, P., Keckhut, P., Trémoulu, S., Listowski, C., Berthet, G., Jégou, F., Khaykin, S., Tidiga, M., and Le Pichon, A.: Case Study of a Mesospheric Temperature Inversion over Maïdo Observatory through a Multi-Instrumental Observation, Remote Sensing, 15, 2045, https://doi.org/10.3390/rs15082045, 2023.

Chanin, M. and Hauchecorne, A.: Lidar observation of gravity and tidal waves in the stratosphere and mesosphere, Journal of Geophysical Research: Oceans, 86, 9715–9721, https://doi.org/10.1029/JC086iC10p09715, 1981.

Chanin, M. L., Garnier, A., Hauchecorne, A., and Porteneuve, J.: A Doppler lidar for measuring winds in the middle atmosphere, Geophysical Research Letters, 16, 1273–1276, https://doi.org/10.1029/GL016i011p01273, 1989.

Chen, C., Chu, X., Zhao, J., Roberts, B. R., Yu, Z., Fong, W., Lu, X., and Smith, J. A.: Lidar observations of persistent gravity waves with periods of 3–10 h in the Antarctic middle and upper atmosphere at McMurdo (77.83°S, 166.67°E), Journal of Geophysical Research: Space Physics, 121, 1483–1502, https://doi.org/10.1002/2015JA022127, 2016.

Duck, T. J., Whiteway, J. A., and Carswell, A. I.: The Gravity Wave–Arctic Stratospheric Vortex Interaction, Journal of the Atmospheric Sciences, 58, 3581–3596, https://doi.org/10.1175/1520-0469(2001)058<3581:TGWASV>2.0.CO;2, 2001.

Eckermann, S. D., Hirota, I., and Hocking, W. K.: Gravity wave and equatorial wave morphology of the stratosphere derived from long-term rocket soundings, Quarterly Journal of the Royal Meteorological Society, 121, 149–186, https://doi.org/10.1002/qj.49712152108, 1995.

Ehard, B., Achtert, P., and Gumbel, J.: Long-term lidar observations of wintertime gravity wave activity over northern Sweden, Annales Geophysicae, 32, 1395–1405, https://doi.org/10.5194/angeo-32-1395-2014, 2014.

Ehard, B., Kaifler, B., Kaifler, N., and Rapp, M.: Evaluation of methods for gravity wave extraction from middle-atmospheric lidar temperature measurements, Atmospheric Measurement Techniques, 8, 4645–4655, https://doi.org/10.5194/amt-8-4645-2015, 2015.

Fritts, D. C. and Alexander, M. J.: Gravity wave dynamics and effects in the middle atmosphere, Reviews of Geophysics, 41, 2001RG000 106, https://doi.org/10.1029/2001RG000106, 2003.

Gantois, D., Payen, G., Sicard, M., Duflot, V., Bègue, N., Marquestaut, N., Portafaix, T., Godin-Beekmann, S., Hernandez, P., and Golubic, E.: Multiwavelength aerosol lidars at the Maïdo supersite, Réunion Island, France: instrument description, data processing chain, and quality assessment, Earth System Science Data, 16, 4137–4159, https://doi.org/10.5194/essd-16-4137-2024, 2024.

Gardner, C. S., Miller, M. S., and Liu, C. H.: Rayleigh Lidar Observations of Gravity Wave Activity in the Upper Stratosphere at Urbana, Illinois, Journal of the Atmospheric Sciences, 46, 1838–1854, https://doi.org/10.1175/1520-0469(1989)046<1838:RLOOGW>2.0.CO;2, 1989.

Gardner, C. S., Hostetler, C. A., and Franke, S. J.: Gravity wave models for the horizontal wave number spectra of atmospheric velocity and density fluctuations, Journal of Geophysical Research: Atmospheres, 98, 1035–1049, https://doi.org/10.1029/92JD02051, 1993.

Geller, M. A. and Gong, J.: Gravity wave kinetic, potential, and vertical fluctuation energies as indicators of different frequency gravity waves, Journal of Geophysical Research: Atmospheres, 115, 2009JD012 266, https://doi.org/10.1029/2009JD012266, 2010.

Guest, F. M., Reeder, M. J., Marks, C. J., and Karoly, D. J.: Inertia–Gravity Waves Observed in the Lower Stratosphere over Macquarie Island, Journal of the Atmospheric Sciences, 57, 737–752, https://doi.org/10.1175/1520-0469(2000)057<0737:IGWOIT>2.0.CO;2, 2000.

Guo, T., Zhang, T., Lim, E., Lopez-Benitez, M., Ma, F., and Yu, L.: A Review of Wavelet Analysis and Its Applications: Challenges and Opportunities, IEEE Access, 10, 58 869–58 903, https://doi.org/10.1109/ACCESS.2022.3179517, 2022.

Hauchecorne, A. and Chanin, M.: Density and temperature profiles obtained by lidar between 35 and 70 km, Geophysical Research Letters, 7, 565–568, https://doi.org/10.1029/GL007i008p00565, 1980.

Hauchecorne, A., Gonzalez, N., Souprayen, C., Manson, A., Meek, C., Singer, W., Fakhrutdinova, A., Hoppe, U.-P., Bosˇka, J., Laštovička, J., Scheer, J., Reisin, E., and Graef, H.: Gravity-wave activity and its relation with prevailing winds during DYANA, Journal of Atmospheric and Terrestrial Physics, 56, 1765–1778, https://doi.org/10.1016/0021-9169(94)90009-4, 1994.

Hersbach, H., Bell, B., Berrisford, P., Hirahara, S., Horányi, A., Muñoz-Sabater, J., Nicolas, J., Peubey, C., Radu, R., Schepers, D., Simmons, A., Soci, C., Abdalla, S., Abellan, X., Balsamo, G., Bechtold, P., Biavati, G., Bidlot, J., Bonavita, M., De Chiara, G., Dahlgren, P., Dee, D., Diamantakis, M., Dragani, R., Flemming, J., Forbes, R., Fuentes, M., Geer, A., Haimberger, L., Healy, S., Hogan, R. J., Hólm, E., Janisková, M., Keeley, S., Laloyaux, P., Lopez, P., Lupu, C., Radnoti, G., De Rosnay, P., Rozum, I., Vamborg, F., Villaume, S., and Thépaut, J.: The ERA5 global reanalysis, Quarterly Journal of the Royal Meteorological Society, 146, 1999–2049, https://doi.org/10.1002/qj.3803, 2020.

Hertzog, A., Souprayen, C., and Hauchecorne, A.: Measurements of gravity wave activity in the lower stratosphere by Doppler lidar, Journal of Geophysical Research: Atmospheres, 106, 7879–7890, https://doi.org/10.1029/2000JD900646, 2001.

Hirota, I.: Climatology of gravity waves in the middle atmosphere, Journal of Atmospheric and Terrestrial Physics, 46, 767–773, https://doi.org/10.1016/0021-9169(84)90057-6, 1984.

Hirota, I. and Niki, T.: A Statistical Study of Inertia-Gravity Waves in the Middle Atmosphere, Journal of the Meteorological Society of Japan. Ser. II, 63, 1055–1066, https://doi.org/10.2151/jmsj1965.63.6_1055, 1985.

Holton, J. R. and Alexander, M. J.: The role of waves in the transport circulation of the middle atmosphere, in: Geophysical Monograph Series, vol. 123, pp. 21–35, American Geophysical Union, Washington, D. C., ISBN 978-0-87590-981-3, https://doi.org/10.1029/GM123p0021, 2000.

Homeyer, C. R. and Bowman, K. P.: Rossby Wave Breaking and Transport between the Tropics and Extratropics above the Subtropical Jet, Journal of the Atmospheric Sciences, 70, 607–626, https://doi.org/10.1175/jas-d-12-0198.1, publisher: American Meteorological Society, 2013.

Hubbard, B. B.: The World According to Wavelets: The Story of a Mathematical Technique in the Making, Second Edition, A K Peters/CRC Press, 0 edn., ISBN 978-0-429-06462-3, https://doi.org/10.1201/9781439864555, 1998.

Kaifler, B., Lübken, F., Höffner, J., Morris, R. J., and Viehl, T. P.: Lidar observations of gravity wave activity in the middle atmosphere over Davis (69°S, 78°E), Antarctica, Journal of Geophysical Research: Atmospheres, 120, 4506–4521, https://doi.org/10.1002/2014JD022879, 2015.

Khaykin, S. M., Hauchecorne, A., Mzé, N., and Keckhut, P.: Seasonal variation of gravity wave activity at midlatitudes from 7 years of COSMIC GPS and Rayleigh lidar temperature observations, Geophysical Research Letters, 42, 1251–1258, https://doi.org/10.1002/2014gl062891, publisher: American Geophysical Union (AGU), 2015.

Khaykin, S. M., Hauchecorne, A., Porteneuve, J., Mariscal, J.-F., D'Almeida, E., Cammas, J.-P., Payen, G., Evan, S., and Keckhut, P.: Ground-Based Rayleigh-Mie Doppler Lidar for Wind Measurements in the Middle Atmosphere, EPJ Web of Conferences, 119, 13 005, https://doi.org/10.1051/epjconf/201611913005, 2016.

Khaykin, S. M., Godin-Beekmann, S., Keckhut, P., Hauchecorne, A., Jumelet, J., Vernier, J.-P., Bourassa, A., Degenstein, D. A., Rieger, L. A., Bingen, C., Vanhellemont, F., Robert, C., DeLand, M., and Bhartia, P. K.: Variability and evolution of the midlatitude stratospheric aerosol budget from 22 years of ground-based lidar and satellite observations, Atmospheric Chemistry and Physics, 17, 1829–1845, https://doi.org/10.5194/acp-17-1829-2017, 2017.

Khaykin, S. M., Hauchecorne, A., Cammas, J.-P., Marqestaut, N., Mariscal, J.-F., Posny, F., Payen, G., Porteneuve, J., and Keckhut, P.: Exploring fine-scale variability of stratospheric wind above the tropical la reunion island using rayleigh-mie doppler lidar, EPJ Web of Conferences, 176, 03 004, https://doi.org/10.1051/epjconf/201817603004, 2018.

Kishore, P., Venkat Ratnam, M., Velicogna, I., Sivakumar, V., Bencherif, H., Clemesha, B. R., Simonich, D. M., Batista, P. P., and Beig, G.: Long-term trends observed in the middle atmosphere temperatures using ground based LIDARs and satellite borne measurements, Annales Geophysicae, 32, 301–317, https://doi.org/10.5194/angeo-32-301-2014, 2014.

Kruse, C. G., Alexander, M. J., Hoffmann, L., Van Niekerk, A., Polichtchouk, I., Bacmeister, J. T., Holt, L., Plougonven, R., Šácha, P., Wright, C., Sato, K., Shibuya, R., Gisinger, S., Ern, M., Meyer, C. I., and Stein, O.: Observed and Modeled Mountain Waves from the Surface to the Mesosphere near the Drake Passage, Journal of the Atmospheric Sciences, 79, 909–932, https://doi.org/10.1175/JAS-D-21-0252.1, 2022.

Li, H., Zhang, J., Sheng, B., Fan, Y., Ji, X., and Li, Q.: The Gravity Wave Activity during Two Recent QBO Disruptions Revealed by U.S. High-Resolution Radiosonde Data, Remote Sensing, 15, 472, https://doi.org/10.3390/rs15020472, 2023.

Li, T., Leblanc, T., McDermid, I. S., Keckhut, P., Hauchecorne, A., and Dou, X.: Middle atmosphere temperature trend and solar cycle revealed by long-term Rayleigh lidar observations, Journal of Geophysical Research, 116, D00P05, https://doi.org/10.1029/2010JD015275, 2011.

Liu, H., Marsh, D. R., She, C., Wu, Q., and Xu, J.: Momentum balance and gravity wave forcing in the mesosphere and lower thermosphere, Geophysical Research Letters, 36, 2009GL037 252, https://doi.org/10.1029/2009GL037252, 2009.

Lu, X., Chu, X., Fong, W., Chen, C., Yu, Z., Roberts, B. R., and McDonald, A. J.: Vertical evolution of potential energy density and vertical wave number spectrum of Antarctic gravity waves from 35 to 105 km at McMurdo (77.8°S, 166.7°E), Journal of Geophysical Research: Atmospheres, 120, 2719–2737, https://doi.org/10.1002/2014JD022751, 2015.

Lu, X., Chu, X., Li, H., Chen, C., Smith, J. A., and Vadas, S. L.: Statistical characterization of high-to-medium frequency mesoscale gravity waves by lidar-measured vertical winds and temperatures in the MLT, Journal of Atmospheric and Solar-Terrestrial Physics, 162, 3–15, https://doi.org/10.1016/j.jastp.2016.10.009, 2017.

Mallat, S.: A theory for multiresolution signal decomposition: the wavelet representation, IEEE Transactions on Pattern Analysis and Machine Intelligence, 11, 674–693, https://doi.org/10.1109/34.192463, 1989.

Medvedev, A. S. and Yiğit, E.: Gravity Waves in Planetary Atmospheres: Their Effects and Parameterization in Global Circulation Models, Atmosphere, 10, 531, https://doi.org/10.3390/atmos10090531, 2019.

Mzé, N., Hauchecorne, A., Keckhut, P., and Thétis, M.: Vertical distribution of gravity wave potential energy from long-term Rayleigh lidar data at a northern middle-latitude site, Journal of Geophysical Research: Atmospheres, 119, https://doi.org/10.1002/2014JD022035, 2014.

Pfenninger, M., Liu, A. Z., Papen, G. C., and Gardner, C. S.: Gravity wave characteristics in the lower atmosphere at south pole, Journal of Geophysical Research: Atmospheres, 104, 5963–5984, https://doi.org/10.1029/98JD02705, 1999.

Picone, J. M., Hedin, A. E., Drob, D. P., and Aikin, A. C.: NRLMSISE-00 empirical model of the atmosphere: Statistical comparisons and scientific issues, Journal of Geophysical Research: Space Physics, 107, https://doi.org/10.1029/2002JA009430, 2002.

Placke, M., Hoffmann, P., Gerding, M., Becker, E., and Rapp, M.: Testing linear gravity wave theory with simultaneous wind and temperature data from the mesosphere, Journal of Atmospheric and Solar-Terrestrial Physics, 93, 57–69, https://doi.org/10.1016/j.jastp.2012.11.012, 2013.

Plougonven, R. and Zhang, F.: Internal gravity waves from atmospheric jets and fronts, Reviews of Geophysics, 52, 33–76, https://doi.org/10.1002/2012RG000419, 2014.

Polichtchouk, I., Wedi, N., and Kim, Y.: Resolved gravity waves in the tropical stratosphere: Impact of horizontal resolution and deep convection parametrization, Quarterly Journal of the Royal Meteorological Society, 148, 233–251, https://doi.org/10.1002/qj.4202, 2022.

Ratynski, M., Khaykin, S., Hauchecorne, A., Wing, R., Cammas, J.-P., Hello, Y., and Keckhut, P.: Validation of Aeolus wind profiles using ground-based lidar and radiosonde observations at Réunion island and the Observatoire de Haute-Provence, Atmos. Meas. Tech., 2023.

Rauthe, M., Gerding, M., and Lübken, F.-J.: Seasonal changes in gravity wave activity measured by lidars at mid-latitudes, Atmospheric Chemistry and Physics, 8, 6775–6787, https://doi.org/10.5194/acp-8-6775-2008, 2008.

Souprayen, C., Garnier, A., Hertzog, A., Hauchecorne, A., and Porteneuve, J.: Rayleigh–Mie Doppler wind lidar for atmospheric measurements I Instrumental setup, validation, and first climatological results, Applied Optics, 38, 2410, https://doi.org/10.1364/AO.38.002410, 1999.

Strelnikova, I., Almowafy, M., Baumgarten, G., Baumgarten, K., Ern, M., Gerding, M., and Lübken, F.-J.: Seasonal Cycle of Gravity Wave Potential Energy Densities from Lidar and Satellite Observations at 54° and 69°N, Journal of the Atmospheric Sciences, 78, 1359–1386, https://doi.org/10.1175/JAS-D-20-0247.1, 2021.

Vadas, S. L., Becker, E., Bossert, K., Baumgarten, G., Hoffmann, L., and Harvey, V. L.: Secondary Gravity Waves From the Stratospheric Polar Vortex Over ALOMAR Observatory on 12–14 January 2016: Observations and Modeling, Journal of Geophysical Research: Atmospheres, 128, e2022JD036 985, https://doi.org/10.1029/2022JD036985, 2023.

Vallis, G. K.: Atmospheric and Oceanic Fluid Dynamics: Fundamentals and Large-Scale Circulation, Cambridge University Press, 2 edn., ISBN 978-1-107-06550-5 978-1-107-58841-7, https://doi.org/10.1017/9781107588417, 2017.

Whiteway, J. A. and Carswell, A. I.: Lidar observations of gravity wave activity in the upper stratosphere over Toronto, Journal of Geophysical Research: Atmospheres, 100, 14 113–14 124, https://doi.org/10.1029/95JD00511, 1995.

Wilson, R., Hauchecorne, A., and Chanin, M. L.: Gravity wave spectra in the middle atmosphere as observed by Rayleigh lidar, Geophysical Research Letters, 17, 1585–1588, https://doi.org/10.1029/GL017i010p01585, 1990.

Wilson, R., Chanin, M. L., and Hauchecorne, A.: Gravity waves in the middle atmosphere observed by Rayleigh lidar: 2. Climatology, Journal of Geophysical Research: Atmospheres, 96, 5169–5183, https://doi.org/10.1029/90JD02610, 1991.

Wüst, S., Küchelbacher, L., Trinkl, F., and Bittner, M.: Gravity waves above the Northern Atlantic and Europe during streamer events using ADM-Aeolus, https://doi.org/10.5194/amt-2024-18, 2024.

Yamashita, C., Chu, X., Liu, H., Espy, P. J., Nott, G. J., and Huang, W.: Stratospheric gravity wave characteristics and seasonal variations observed by lidar at the South Pole and Rothera, Antarctica, Journal of Geophysical Research: Atmospheres, 114, 2008JD011 472, https://doi.org/10.1029/2008JD011472, 2009.